

## 174P/Echeclus and its Blue Coma Observed Post-Outburst

TOM SECCULL,<sup>1</sup> WESLEY C. FRASER,<sup>1</sup> THOMAS H. PUZIA,<sup>2</sup> ALAN FITZSIMMONS,<sup>1</sup> AND GUIDO CUPANI<sup>3</sup>

<sup>1</sup> *Astrophysics Research Centre, Queen's University Belfast, University Road, Belfast, BT7 1NN, UK*

<sup>2</sup> *Institute of Astrophysics, Pontificia Universidad Católica de Chile, Av. Vincuña Mackenna 4860, 7820436, Santiago, Chile*

<sup>3</sup> *INAF — Osservatorio Astronomico di Trieste, via G. B. Tiepolo 11, I-34143, Trieste, Italy*

(Received Nov 30, 2018; Revised ...; Accepted ...)

Submitted to AJ

### ABSTRACT

It has been suggested that centaurs may lose their red surfaces and become bluer due to the onset of cometary activity, but the way in which cometary outbursts affect the surface composition and albedo of active centaurs is poorly understood. We obtained consistent visual-NIR reflectance spectra of the sporadically active centaur 174P/Echeclus during a period of inactivity in 2014 and six weeks after its outburst in 2016 to see if activity had observably changed the surface properties of the nucleus. We observed no change in Echeclus' surface reflectance properties following the outburst compared to before, indicating that, in this case, any surface changes due to cometary activity were not sufficiently large to be observable from Earth. Our spectra and post-outburst imaging have revealed, however, that the remaining dust coma is not only blue compared to Echeclus, but also bluer than Solar, with a spectral gradient of  $-7.7 \pm 0.6\%$  per  $0.1 \mu\text{m}$  measured through the  $0.61 - 0.88 \mu\text{m}$  wavelength range that appears to continue up to  $\lambda \sim 1.3 \mu\text{m}$  before becoming neutral. We conclude that the blue visual colour of the dust is likely not a scattering effect, and instead may be indicative of the dust's carbon-rich composition. Deposition of such blue, carbon-rich, comatic dust onto a red active centaur may be a mechanism by which its surface colour could be neutralised.

*Keywords:* comets: general — comets: individual: (60558) 174P/Echeclus — Kuiper belt: general

### 1. INTRODUCTION

Centaurs are a population of minor planetary objects that currently reside amongst the outer planets of the Solar System; their orbits are typically defined by a perihelion greater than Jupiter's semimajor-axis ( $q > 5.2 \text{ au}$ ) and a semimajor-axis smaller than that of Neptune ( $a < 30.1 \text{ au}$ ; Gladman et al. 2008). Most centaurs are thought to originate in the Trans-Neptunian Belt's Scattered Disk, before gravitational interaction with Neptune forces their orbits to cross those of the giant planets (Levison & Duncan 1997; Duncan et al. 2004; Gomes et al. 2008). Such orbits are unstable with dynamical lifetimes of only order  $\sim 10^6 - 10^7$  years (Levison & Duncan 1997; Dones et al. 1999; Tiscareno & Malhotra 2003; Horner et al. 2004; Di Sisto & Brunini

2007). Gravitational planetary interactions can result in their ejection from the Solar System (Tiscareno & Malhotra 2003), or the evolution of their orbits into those of Jupiter Family Comets (JFCs; Duncan et al. 2004). As centaurs migrate toward the inner Solar System, experiencing higher temperatures, some exhibit the onset of cometary activity. It has been suggested that cometary activity should cause the surfaces of red centaurs to change, such that they no longer look like red Trans-Neptunian Objects (TNOs), and instead look more similar to the neutrally coloured JFCs (Luu & Jewitt 1996; Jewitt 2002, 2015; Lamy & Toth 2009).

Around 13% of known centaurs have been observed to show cometary activity (Jewitt 2009). From in-situ observations of the active JFC 67P/Churyumov-Gerasimenko (hereafter 67P) made by the European Space Agency's Rosetta spacecraft, it is known that cometary activity changes the surface properties of a cometary nucleus. Filacchione et al. (2016a) reported

that at 67P Rosetta's VIRTIS instrument observed the single scattering albedo of active areas increasing, and their spectral slopes decreasing, suggesting that cometary outgassing was lifting redder dust from the surface to reveal more reflective and bluer subsurface water ice. The increase in surface water ice abundance was also observed in reflectance spectra of the active regions by the increasing depth of an absorption feature observed at  $\lambda \sim 3.2 \mu\text{m}$ , and the distortion of its centre toward shorter wavelengths (Filacchione et al. 2016a). While these changes are clear in the measurements of 67P, they have not yet been observed on an active centaur's surface.

Plausible evidence for centaur surface changes due to activity come from hemispherically-averaged color measurements. The colors (or spectral slopes) of centaurs are bimodally distributed into a red group and a less-red group (Peixinho et al. 2003; Barucci et al. 2005; Tegler et al. 2008; Perna et al. 2010) but active centaurs have only been observed within the less-red group (Jewitt 2009). Red surfaces are also reported to be less common on centaurs with perihelia below  $\sim 10$  au; this heliocentric distance roughly coincides with that where activity is observed to begin (Jewitt 2015). It has been argued that activity can destroy a centaur's original red irradiated crust and resurface it with less-red unirradiated subsurface material that falls back from the coma under gravity (Jewitt 2002; Delsanti et al. 2004; Doressoundiram et al. 2005). Despite this apparent trend for activity causing bluing of a centaur's spectrum, no changes in their surface spectral properties have been directly detected following observed activity.

174P/Echeclus (also known as (60558) Echeclus, formerly known as 2000 EC<sub>98</sub>; Scotti et al. 2000, and hereafter simply referred to as Echeclus) is a centaur that has been extensively studied while both inactive and active. Its orbit ( $a=10.68$  au,  $e=0.46$ ,  $i=4.34^\circ$ ,  $q=5.82$  au,  $t_q=2015$  Apr 22)<sup>1</sup> has been described as "Jupiter coupled" by Gladman et al. (2008), whose numerical integrations found Echeclus to be rapidly perturbed by Jupiter. Echeclus is in the less-red group of centaurs, and slope measurements obtained for the featureless visual spectrum of its bare nucleus are consistent, at  $\sim 10 - 13\%$  per  $0.1 \mu\text{m}$  (Boehnhardt et al. 2002; Bauer et al. 2003b; Alvarez-Candal et al. 2008; Stansberry et al. 2008; Peixinho et al. 2015). A NIR spectrum of Echeclus reported by Guillet et al. (2009) has a low spectral slope of  $2.53 \pm 0.33\%$  per  $0.1 \mu\text{m}$ , and no water ice absorption features.

Since its discovery Echeclus has been observed outbursting four times. The first, discovered by Choi et al. (2006a), was a large outburst that occurred in 2005 December. Two minor outbursts occurred in 2011 May (Jaeger et al. 2011) and 2016 August (Miles et al. 2016). Most recently another large outburst was discovered in 2017 December by amateur astronomers<sup>2</sup>. Multiple works have been published on Echeclus' outburst of 2005-2006, which was one of the largest centaur outbursts ever observed. Persisting for several months, it rose in visual magnitude from  $\sim 21$  to  $\sim 14$  (Rousselot 2008). Unusually, the source of activity appeared to be distinct from Echeclus itself, and was possibly a fragment of the nucleus broken off by the outburst (Choi et al. 2006b; Weissman et al. 2006; Bauer et al. 2008; Rousselot 2008; Fernández 2009). Both Bauer et al. (2008) and Rousselot (2008) reported high dust production rates, low gas-dust ratios, and dust colors redder than Solar but more neutral than Echeclus itself. These dust colour properties were also apparent in observations of Echeclus' 2011 outburst (Rousselot et al. 2016) and have been attributed to dust grain size and scattering effects (Bauer et al. 2008; Rousselot 2008; Rousselot et al. 2016). While Echeclus' outbursts (and CO outgassing; Wierzchos et al. 2017) have received much attention, any effects of an outburst on this centaur's surface composition have not been reported.

In 2014 August we obtained a high quality visual-NIR (VNIR) spectrum of Echeclus' bare nucleus as part of a program observing centaurs and TNOs with the X-Shooter spectrograph (Vernet et al. 2011), mounted on the European Southern Observatory's (ESO's) Very Large Telescope (VLT). Echeclus unexpectedly outburst on 2016 August 27 at a heliocentric distance of 6.27 au; it increased in brightness by 2.6 magnitudes in  $r'$  in less than a day (Miles et al. 2016). Additional spectra of similarly high quality were gathered in early October 2016, six weeks after outburst, to enable a direct measure of any new absorption features, changes in Echeclus' visual and NIR spectral slopes, and the colour of any residual dust coma. We discuss both sets of observations, and provide interpretation below.

## 2. OBSERVATIONS

Echeclus was observed during two epochs (before and after the 2016 outburst) using the X-Shooter spectrograph at ESO's VLT. Pre-outburst observations were performed in visitor mode on 2014 August 3, and post-outburst observations were performed in service mode over two nights on 2016 October 7-8. Our observations

<sup>1</sup> Orbital elements from the IAU Minor Planet Center

<sup>2</sup> <https://www.britastro.org/node/11931>

**Table 1.** Spectroscopy Observation Details

Target	Observation Date   UT Time	Exposure Time (s)			Exposures	Airmass	Seeing (")
<b>Pre-Outburst</b>							
		UVB	VIS	NIR			
HD 198289	2014-08-03   04:21:28 - 04:27:35	3.0	3.0	12.0	3	1.020 - 1.023	0.68 - 0.94
HD 198289	2014-08-03   04:31:56 - 04:38:05	10.0	10.0	40.0	3	1.018 - 1.019	0.62 - 0.83
Echeclus	2014-08-03   05:16:05 - 07:24:17	500.0	466.0	532.0	12	1.022 - 1.259	0.67 - 1.60
HIP 107708	2014-08-03   07:50:27 - 07:56:29	6.0	6.0	24.0	3	1.141 - 1.161	1.24 - 1.42
HIP 105408	2014-08-03   08:04:25 - 08:10:55	10.0	10.0	40.0	3	1.304 - 1.329	1.20 - 1.70
<b>Post-Outburst</b>							
HIP 107708	2016-10-07   04:29:03 - 04:35:02	6.0	6.0	24.0	3	1.336 - 1.371	0.54 - 0.64
Echeclus	2016-10-07   04:53:03 - 05:51:00	500.0	466.0	532.0	6	1.159 - 1.211	0.39 - 0.64
HD 16017	2016-10-07   06:20:03 - 06:23:02	6.0	6.0	24.0	3	1.154 - 1.155	0.45 - 0.55
HIP 107708	2016-10-08   04:04:17 - 04:35:02	6.0	6.0	24.0	3	1.249 - 1.278	0.59 - 0.75
Echeclus	2016-10-08   04:35:56 - 05:33:47	500.0	466.0	532.0	6	1.158 - 1.191	0.44 - 0.75
HD 16017 <sup>a</sup>	2016-10-08   05:53:55 - 05:59:56	6.0	6.0	24.0	2	1.154 - 1.156	0.36 - 0.41

NOTE—<sup>a</sup> This triplet of exposures could not be completed due to time constraints.

were designed to be the same in both epochs; this is the case unless otherwise specified.

X-Shooter is a medium resolution echelle spectrograph with three arms that can be exposed simultaneously, covering the near-UV/blue (UVB; 0.30—0.56  $\mu\text{m}$ ), visual (VIS; 0.55—1.02  $\mu\text{m}$ ) and NIR (1.02—2.48  $\mu\text{m}$ ) spectral ranges (Vernet et al. 2011). While our pre-outburst observations used X-Shooter’s full wavelength coverage, we used its K-band blocking filter for our post-outburst observations. This filter blocks incoming flux at wavelengths longer than 2.1  $\mu\text{m}$  while boosting the signal-to-noise ratio (S/N) in the rest of the NIR spectrum. The UVB, VIS, and NIR detectors have respective pixel scales of 0.16'', 0.16'' and 0.21''. We set the UVB, VIS, and NIR slits to widths of 1.0'', 0.9'' and 0.9'', each providing a respective resolving power of  $\sim$ 5400,  $\sim$ 8900 and  $\sim$ 5600. The slits for each arm have a common length of 11''. No readout binning was performed for any of the observations.

The spectra were observed in a 3 point dither pattern to mitigate bad pixel artifacts and cosmic ray contamination. The slit was realigned to the parallactic angle at the beginning of each triplet to reduce the effects of atmospheric differential refraction; this was especially important because X-Shooter’s Atmospheric Dispersion Corrector (ADC) was disabled during both observing runs. During the pre-outburst run three solar calibrator stars were observed with the same instrument setup, adjacent in time to Echeclus, and at similar airmass: these included HD 198289, Hip 107708 and Hip 105408. Similarly, two calibrator stars were observed on each night during the post-outburst run, Hip 107708 and HD 16017.

We ensured that at least one star, Hip 107708, was common to both observing runs so a direct comparison could be made between the pre- and post-outburst reflectance spectra. During the pre-outburst run, flux calibrators EG 274 and Feige 110 were observed as part of the standard X-Shooter calibration program; similarly, flux standards LTT 3218 and LTT 7987 were observed during the post-outburst run (Vernet et al. 2010). Further spectroscopic observation details are reported in Table 1.

X-Shooter also has a limited imaging mode (Martayan et al. 2014), which we used to study Echeclus’ coma. This imaging mode uses X-Shooter’s Acquisition and Guiding Camera (AGC) which has a  $512 \times 512$  pixel E2V broad band coated CCD, a  $1.5' \times 1.5'$  field of view, a pixel scale of  $\sim$ 0.17'' and a number of standard photometric filters. On the first night of the post-outburst observing run three images were obtained in both SDSS g' and r' filters, one each of exposure length 5s, 15s, and 45s (see Fig. 1).

### 3. DATA REDUCTION

#### 3.1. Spectra: Echeclus

Standard reduction steps (including order rectification and merging, and flux calibration) were performed for all the observed Echeclus and calibrator spectra with ESO’s X-Shooter data reduction pipeline (v. 2.7.1; Modigliani et al. 2010) in the ESO Reflex data processing environment (v. 2.8.4; Freudling et al. 2013). Sky subtraction, cosmic ray removal and extraction of Echeclus’ spectrum was performed in a similar manner to that described in more detail by Seccull et al. (2018). Briefly, Moffat functions (Moffat 1969) were fitted to the spatial profile of

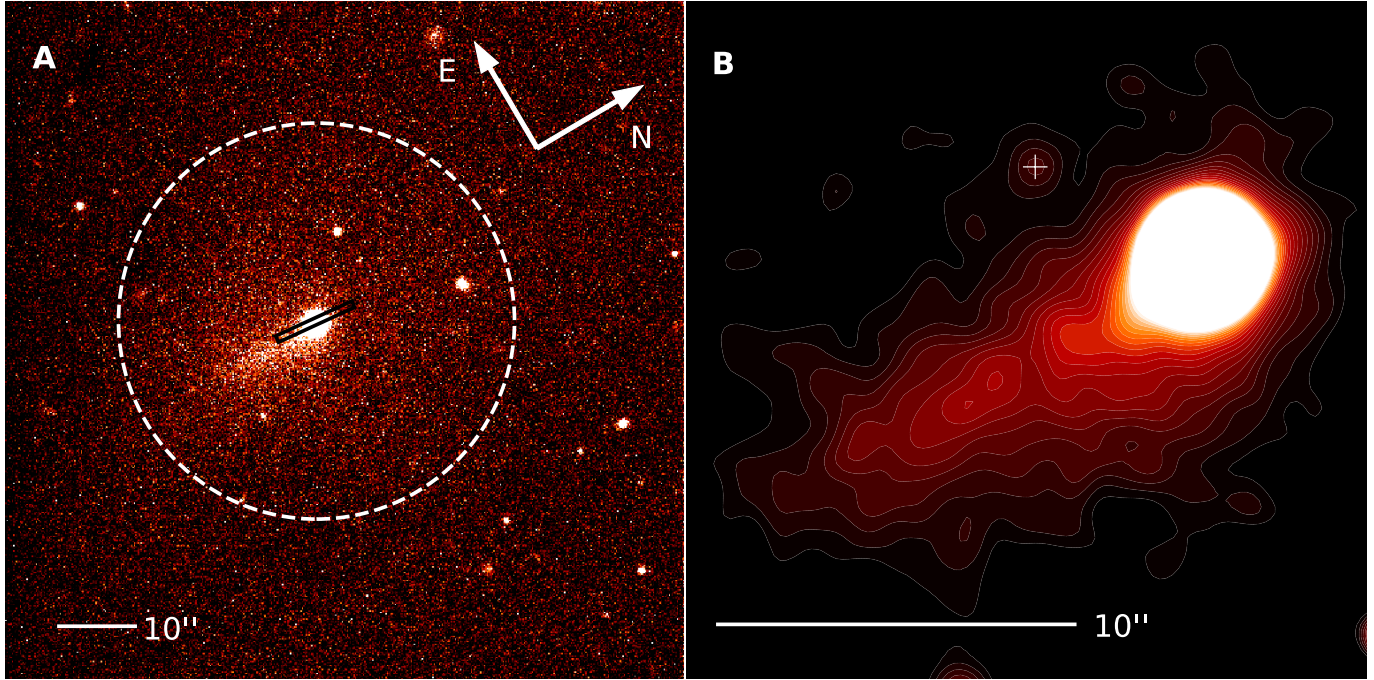


**Figure 1.** Panel A shows a debiased, flat-fielded, 45 second  $r'$  exposure of Echeclus and its coma, observed with X-Shooter’s AGC on 2016 Oct 7. The dashed ring has a radius of  $26''$  ( $\sim 1 \times 10^5$  km at Echeclus) and is centered on the nucleus, marking the point at which the radially averaged surface brightness of the coma blends into that of the background sky. The small black rectangle marks the size and average orientation of X-Shooter’s slit while obtaining spectra of Echeclus on 2016 Oct 7. Panel B shows a zoomed contour plot of the same image after it was smoothed with a gaussian filter. It has linear scaling, and shows the observed morphology of Echeclus’ coma, which is similar to that observed in our  $g'$  image on the same night. The lowest contour is set at one standard deviation of the background noise above the median background level. A + symbol marks a background source that is unrelated to Echeclus.

the 2D rectified and merged spectrum at many locations along the dispersion axis in order to track the wavelength dependent center and width of the spectrum’s spatial profile. Sky region boundaries were defined at  $\pm 3$  Full-Widths at Half Maximum (FWHM) from each Moffat profile center with sky outside these boundaries. Cosmic rays in the sky and target regions were separately sigma clipped at  $5\sigma$ . In each unbinned wavelength element the sky and dust flux contribution was subtracted with a linear fit. Another round of Moffat fitting was conducted for the sky-subtracted spectrum and extraction limits were defined at  $\pm 2$  FWHM from each of the Moffat profile centers. Within these limits the flux was summed for each wavelength element to form the 1D spectrum. Following extraction, the individual spectra were median stacked, solar calibrated, and binned. In each bin the data points were sigma clipped at  $3\sigma$  to minimise skew from outlying points; the remaining points were bootstrapped 10<sup>3</sup> times to produce a distribution of medians and standard deviations for the bin. The mean of the distribution of medians was taken as the bin value and the mean of the distribution of standard deviations was used to calculate the bin’s standard error, which was taken as the bin’s uncertainty. Dithers

with low S/N or large residuals following sky subtraction were omitted from the final stack.

While the above extraction method is good for extracting spectra of faint sources (e.g. Fitzsimmons et al. 2018; Seccull et al. 2018), it cuts off the overlapping ends of each spectral arm where X-Shooter’s dichroics reduce the S/N of the spectrum to a point where it is too low to properly extract; this makes alignment of spectra in neighbouring arms a non-trivial task in some cases. The UVB and VIS spectra were simply aligned via a linear fit through the spectral ranges adjacent to the join between them. In all the VIS arm reflectance spectra there is a strong telluric residual feature at 0.9–0.98  $\mu\text{m}$  (see Smette et al. 2015). This produced a large enough gap in usable continuum between the VIS and NIR spectra that we chose not to attempt to align the VIS and NIR arms. Hence, in the following analysis, we consider the combined UVB-VIS spectrum, and the NIR spectrum separately.

All the spectra have been cut below 0.4  $\mu\text{m}$  due to strong residuals caused by differences in metallicity between the Sun and the calibrator stars used (see Hardorp 1980). The spectra have also been cut above 2.1  $\mu\text{m}$  where the sky subtraction was very poor. Di-

rect comparison of the pre- and post-outburst spectra is also not possible at wavelengths above  $2.1\text{ }\mu\text{m}$  due to the K-blocking filter used in the post-outburst observations.

### 3.2. Spectra: Dust

As discussed in Section 2, Echeclus was observed in a three point dither pattern. In the first dither position Echeclus was centered in the slit. In the second and third dithers Echeclus was positioned respectively at  $+2.5''$  and  $-2.5''$  along the slit relative to the center. Due to the asymmetry of the coma and the convenient orientation of the slit on the sky during the post-outburst observations, one end of the slit sampled the dust coma while the other was dominated by sky (see Fig. 1). This made the VNIR extraction of a dust spectrum possible. To extract the dust spectrum we used only the spectra acquired at the second and third dither positions, to extract the dust and the sky spectra, respectively.

The post-outburst 2D rectified and merged spectra produced by the ESO pipeline, and the sky boundaries drawn by the extraction process described in Section 3.1 were used to sky-subtract and extract the spectrum of the coma. The sky region for each dust spectrum was defined in the third dither in a triplet, on the dust-free side of the spectral image at  $>3$  FWHM from the center of Echeclus' spatial profile. Likewise, the dust region in each triplet was defined in the second dither, on the dusty side of the spectral image at  $>3$  FWHM from the center of Echeclus' spatial profile. A sky spectrum was produced for each triplet by taking a median of the pixels in each wavelength element in the 2D sky region. This sky spectrum was then subtracted from the second dither 2D spectrum, and pixels in each wavelength element in the dust region were summed to produce a sky-subtracted 1D dust spectrum. As a result of summing only the flux at  $>3$  FWHM from Echeclus' nucleus the contamination of the dust spectrum by that of Echeclus itself is expected to be minimal.

Like the spectra of the nucleus, the 4 resulting dust spectra were stacked, solar calibrated, and binned. The uncertainties in each spectral bin were determined in the same way as for those in the spectrum of Echeclus (see Section 3.1). The dust reflectance spectrum appears to have a nearly linear behavior through the VNIR range (from  $\sim 0.4\text{--}1.3\text{ }\mu\text{m}$ ; see Fig. 3) and so we were able to align the UVB, VIS and NIR spectra by aligning the UVB and NIR spectra to a linear fit of the VIS spectrum. The dust spectrum was cut above  $1.76\text{ }\mu\text{m}$  where S/N is extremely low.

### 3.3. Images

There is no dedicated data reduction pipeline for images observed by X-Shooter's AGC, so we debiased and

flat-fielded the images using custom scripts written in Python v. 2.7.13<sup>3</sup>. Bias frames were median stacked to make a master bias frame, which was subtracted from the sky-flats and the image. The bias-subtracted sky-flats were averaged, normalised, and divided from the image to flat-field it. It should be noted that the quality of the flat-field was moderately poor towards the edges of the image. The calibrated image was sky-subtracted with TRIPPY (Fraser et al. 2016).

From the post-outburst images we aimed to study Echeclus' remaining dust coma, and to maximise the S/N we chose to only use those with the longest exposure time of 45s in  $g'$  and  $r'$  filters. Due to the very small field of view of X-Shooter's AGC ( $1.5'\times 1.5'$ ), we were limited in the number of sources we could use to calculate the zero-point of the images. Cross-referencing them with the catalogs of the Sloan Digital Sky Survey (SDSS; Abolfathi et al. 2018) and the Panoramic Survey Telescope and Rapid Response System (Pan-STARRS; Flewelling et al. 2016) revealed that they contained only one usable stellar source, as all others beside Echeclus were galaxies. In  $g'$  the uncertainty in the star's magnitude was significant ( $\sim 0.13$  magnitudes) and an accurate zero-point for this image could not be determined; as a result the colors determined for Echeclus and its coma also have significant uncertainty. To determine  $Af\rho$  and a lower limit on the mass of the coma we were limited to using only the  $r'$  image. The uncertainty in all subsequent photometric measurements is dominated by the uncertainty in the measured zero-points.

## 4. RESULTS & ANALYSIS

For Echeclus we obtained 3 reflectance spectra in both the visual (combined UVB+VIS arms) and NIR ranges (see Fig. 2). In each range we obtained one pre-outburst baseline spectrum and two post-outburst spectra. We also obtained one full VNIR spectrum of Echeclus' dust coma from the combined post-outburst observations (see Fig. 3). Prior to the solar calibration of our data we searched the spectra for cometary emission lines that might have indicated ongoing activity, but found none above the level of the noise.

In each reflectance spectrum we measured the spectral gradient,  $S'$ . For each point in a binned spectrum we took its constituent set of unbinned values; these values were bootstrapped allowing for repeats, and were then rebinned. This was done  $10^3$  times for every point in the binned spectrum to produce  $10^3$  sample binned spectra, on each of which a linear regression was performed to create a distribution of  $10^3$  spectral slopes.  $S'$

<sup>3</sup> <https://www.python.org/>

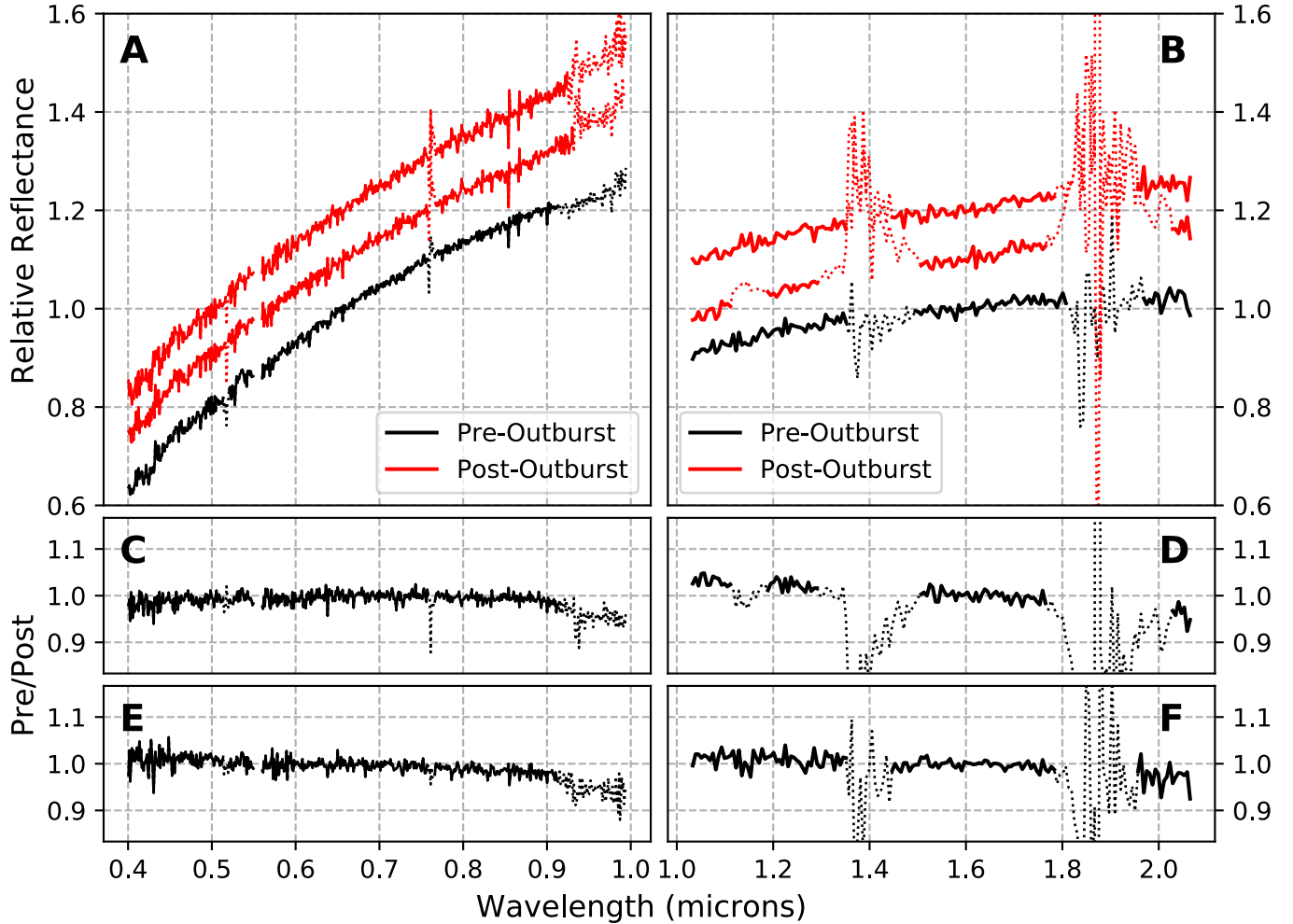


**Figure 2.** Reflectance spectra and ratioed spectra of Echeclus' surface from both observing epochs. All panels on the left (A,C,E) show the visual range and are normalised at  $0.658\text{ }\mu\text{m}$ , while those on the right (B,D,F) display the NIR and are normalised at  $1.6\text{ }\mu\text{m}$ . In all panels y-axis scaling is the same, and spectral regions contaminated by telluric or solar metallicity residuals are plotted with dotted lines. (A,B) In panels A and B the reflectance spectra of Echeclus' surface are shown, with each spectrum ordered from bottom to top in order of when they were observed, and offset for clarity by  $+0.1$  with respect to the previous spectrum. During both observing epochs Echeclus' visual spectrum is featureless and no statistically significant change in the spectral gradient is observed; the same is observed in the NIR. The differing strength and width of the telluric residual bands are related to the difference in airmass at which Echeclus and the calibrator star were observed on a given night (see Table 1). All spectra displayed have been calibrated using the spectrum of Hip 107708. (C-F) The ratioed spectra in panels C and D were created by dividing the reflectance spectra from 2014-08-03 by those from 2016-10-07. The same applies to panels E and F where we used spectra from 2014-08-03 and 2016-10-08. See Section 4.1 for discussion of the ratioed spectra.

was defined as the mean of this slope distribution; standard error of the mean at 99.7% confidence was also recorded (see Table 2). The S' standard errors are very small (0.01% per  $0.1\text{ }\mu\text{m}$ ) and do not account for systematic errors of order 0.5% per  $0.1\text{ }\mu\text{m}$  introduced by imperfect calibration of the data; these systematics can be seen in the curvature and slopes of the ratioed spectra displayed in Fig. 2. Hence we report the measured uncertainty of 0.01% per  $0.1\text{ }\mu\text{m}$  as the limit of precision obtainable from our continuum measurements of these

spectra. The uncertainties quoted in Table 2. do not include the systematic errors.

#### 4.1. Spectra: Echeclus

We observed no appreciable change in the reflectance properties of Echeclus' nucleus post-outburst compared to our pre-outburst baseline spectrum; no observable ice or silicate absorption features have appeared, nor has the shape of the spectrum itself altered.

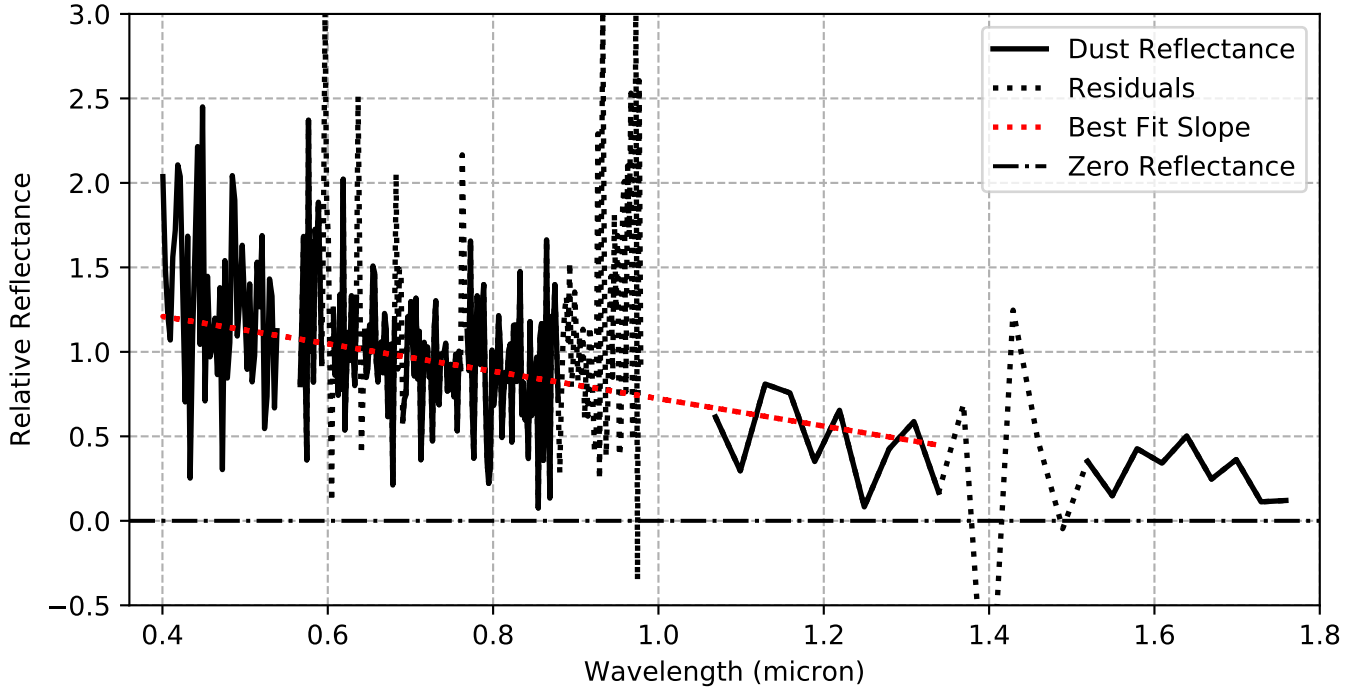


**Figure 3.** The blue, featureless reflectance spectrum of Echeclus' dust coma observed post-outburst. The spectrum is normalised at  $0.658\text{ }\mu\text{m}$ . Dotted lines indicate regions of telluric residuals and systematic residuals produced by very low S/N at the ends of X-Shooter's echelle orders. The red dotted line plots the measured best-fit slope of  $-7.7 \pm 0.6\%$  per  $0.1\text{ }\mu\text{m}$  across the  $0.40\text{--}1.35\text{ }\mu\text{m}$  range (see Section 4.2). The black dot-dash line at zero reflectance indicates the lower limit of the plot where reflectances are still physical. This spectrum was also calibrated using that of Hip 107708.

Ratioed spectra were produced to probe for changes in Echeclus' reflectance properties (see Fig. 2). They show very slight curvature in the visual range. At longer wavelengths they have a small negative gradient. These residual features are not significant, producing maximum residual spectral gradients of order 0.5% per  $0.1\text{ }\mu\text{m}$ . These residual features are likely not intrinsic to Echeclus, but instead are the result of strong telluric residual contamination and systematic errors introduced by imperfect calibration.

In the visual spectra the pre-outburst slope was measured at  $0.575\text{--}0.800\text{ }\mu\text{m}$  while ignoring the telluric residuals at  $0.758\text{--}0.767\text{ }\mu\text{m}$ . Visual S' values and their uncertainties are presented in Table 2. The visual spectral gradients reported here are all consistent with literature values previously published for Echeclus when systematic errors are accounted for (Alvarez-Candal et al. 2008; Stansberry et al. 2008; Peixinho et al. 2015).

To enable direct comparison between our NIR S' measurements, we measured the slope in the wavelength range  $1.25\text{--}1.7\text{ }\mu\text{m}$ , but only in regions with minimal telluric residual contamination due to atmospheric  $\text{H}_2\text{O}$  (see Smette et al. 2015). Hence, we only included data in the ranges  $1.25\text{--}1.3\text{ }\mu\text{m}$  and  $1.5\text{--}1.7\text{ }\mu\text{m}$  in our measurements. Outside of these regions even subtle telluric

**Table 2.** Surface Reflectance Spectrum Gradients

Obs Date	S'	Standard Error <sup>a</sup>
	(% per $0.1\text{ }\mu\text{m}$ )	(% per $0.1\text{ }\mu\text{m}$ )
Visual		
2014-08-03	11.64	$\pm 0.01$
2016-10-07	11.39	$\pm 0.01$
2016-10-08	12.12	$\pm 0.01$
NIR		
2014-08-03	1.26	$\pm 0.01$
2016-10-07	1.69	$\pm 0.01$
2016-10-08	1.34	$\pm 0.01$

NOTE—<sup>a</sup> to account for systematic errors increase these values by 0.5% per  $0.1\text{ }\mu\text{m}$

residuals were able to affect S', despite their apparent absence from the spectrum. At  $\lambda < 1.2\text{ }\mu\text{m}$  the slope of Echeclus' NIR spectrum begins to increase towards the visual range and drops away from linearity; this is why we did not include these wavelengths in our measurements of S'. NIR S' values and their uncertainties are also presented in Table 2. The NIR spectral gradients are broadly neutral like that reported by Guilbert et al. (2009), but our measured values are not formally

consistent with theirs. Due to the significant difference between the wavelength range measured in that study and this one, however, they are not directly comparable.

Taking into account both the formal and systematic uncertainties in our measurements of  $S'$ , we cannot report any changes in observed visual or NIR spectral gradients between the pre- and post-outburst epochs that are attributable to changes in the reflectance properties of Echeclus.

#### 4.2. Spectra: Dust

The reflectance spectrum of Echeclus' dust coma appears entirely featureless, but surprisingly blue in the visual range. Using the same method outlined above we measured the spectrum's gradient,  $S'$ , in the highest S/N region of the VIS dust spectrum (0.61-0.88  $\mu\text{m}$ ), while ignoring regions containing telluric and calibration residuals. We measured the gradient of the VIS dust spectrum and standard error at 99.7% confidence to be  $-7.7 \pm 0.4\%$  per 0.1  $\mu\text{m}$ . Adding 0.5% per 0.1  $\mu\text{m}$  to the slope uncertainty in quadrature to account for systematic errors results in a final slope measurement of  $-7.7 \pm 0.6\%$  per 0.1  $\mu\text{m}$ . The spectrum is broadly linear and appears to have a constant gradient from 0.4-1.3  $\mu\text{m}$ , while leveling out at longer wavelengths.

#### 4.3. Photometry

From our  $g'$  and  $r'$  images we attempted to study Echeclus' dust coma. Following the calibrations described in Section 3.3, the locations of sources in the image were found using SExtractor (Bertin & Arnouts 1996) and using the single stellar source available, a stellar PSF was fitted by TRIPPy (Fraser et al. 2016); TRIPPy was also used for all subsequent photometric measurements. The pixel values of three bright sources close to Echeclus in the image were replaced with values randomly sampled from a gaussian distribution calculated from the median and standard deviation of the background local to each star; this removed these sources from the image while preserving the background coma.

We measured the  $g' - r'$  colors of Echeclus and its coma. First, to measure the color of Echeclus we performed aperture photometry with a circular aperture of radius,  $\rho = 0.45''$ , equal to 1 FWHM of the seeing disk. This aperture was chosen to probe the color of the nucleus and minimise coma contamination. Second, to measure the color of the coma, photometry was performed for a ring centered on the photocenter of Echeclus with an inner bound at  $\rho = 1.35''$  (3 FWHM of Echeclus' seeing disk) and an outer bound at  $\rho = 26''$ ; this included most of Echeclus' observable coma, but

minimised contamination by flux from the nucleus. For Echeclus and its coma we respectively measured  $g' - r'$  colors of  $0.65 \pm 0.14$  and  $0.32 \pm 0.14$ , where the uncertainties are dominated by the uncertainty introduced by the zero-point calibration of the  $g'$  image. Despite the large uncertainty in these color measurements, the colors of Echeclus and its dust coma are not consistent. Importantly, the coma's color is neutral-blue (the Sun has  $g' - r' = 0.44 \pm 0.02$ <sup>4</sup> while Echeclus is red, just as observed in our spectroscopic measurements. These colors, primarily due to their very large uncertainties, are also consistent with the spectral slopes determined from the X-Shooter spectra presented in Table 2, with the colors of Echeclus and the coma respectively corresponding to slopes of approximately  $\sim 12\%$  per 0.1  $\mu\text{m}$  and  $\sim -8\%$  per 0.1  $\mu\text{m}$ .

Next, we determined the radially averaged Surface Brightness Profile (SBP) of Echeclus by measuring the surface brightness of concentric rings centered on the Echeclus' photocenter; the rings had constant width and monotonically increasing radius,  $\rho$ . Here we only used the  $r'$  image due to its higher precision zero-point calibration. The SBP of Echeclus plus its coma is displayed in Figure 4. To study the coma on its own we had to disentangle the SBP of the coma from that of the nucleus, which we have assumed to be the same as a stellar Point Spread Function (PSF). To remove the SBP of the nucleus we broadly followed the procedure described by Kulyk et al. (2016), first normalising both Echeclus' SBP and the SBP of the stellar PSF we previously saved. The SBPs were normalised to 1 at their peaks and to 0 in their wings; in both cases the wings were normalised to the median surface brightness in the region  $26'' < \rho < 30''$ , after the points in that region were sigma-clipped at  $3\sigma$ . Beyond  $\rho \sim 26''$  the surface brightness of the coma blends into that of the background sky (see Figs. 1 & 4).

In each concentric ring of area  $A$  (measured in square arcseconds), the total flux  $F_T$  is the sum of the flux from the nucleus  $F_N$  and flux from the coma  $F_C$ , and surface brightness is given by  $\sigma = (F/A)$ . Assuming the flux contribution from the coma is negligible close to the nucleus, the ratio of nucleus surface brightness to that of total surface brightness in each ring is equal to the proportion of total flux contributed by the nucleus, or  $\sigma_N/\sigma_T = F_N/F_T$ . Therefore in each ring,  $F_N = F_T(\sigma_N/\sigma_T)$  and  $F_C = F_T(1 - (\sigma_N/\sigma_T))$ . From here we can use the normalised Echeclus-plus-coma SBP and the normalised stellar SBP to determine the rela-

<sup>4</sup> <https://www.sdss.org/dr12/algorithms/ugrizvegasun/>

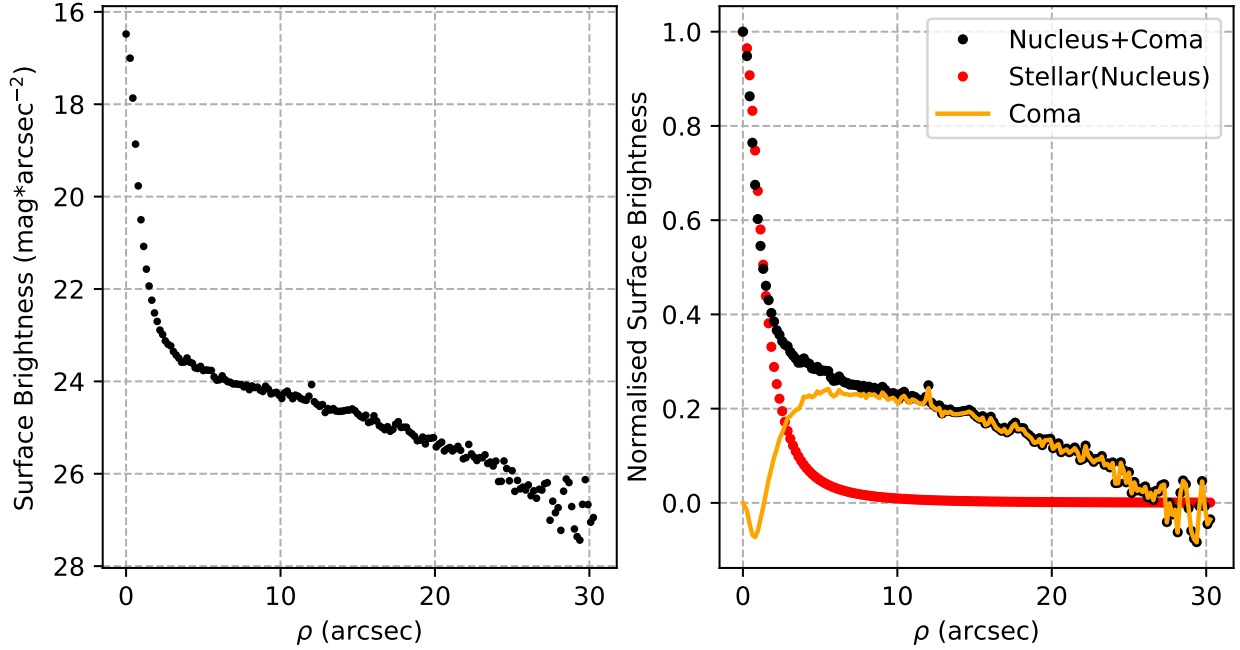


**Figure 4.** Radially averaged surface brightness profiles (SBPs) of Echeclus produced from our single usable  $r'$  image. (**Left**) The SBP of Echeclus given in magnitudes per arcsec<sup>2</sup>. Errorbars are present in this plot but are smaller than the plotted points. As explained in the text the photometric uncertainties should be considered larger than they are presented here, due to the poor flat-field calibration of the image. (**Right**) The SBP of Echeclus normalised to one at its peak and to zero in the wings is shown with the normalised SBP calculated from a single fitted stellar PSF which we use as a proxy for the SBP of Echeclus' bare nucleus. The normalised SBP of the coma, produced by subtracting the stellar profile from the total profile, is also presented. The negative coma SBP at small  $\rho$  is caused by the stellar SBP being wider than the total SBP close to the nucleus.

tive contributions to flux from the nucleus and coma in each ring (see Fig. 4). With a photometric aperture of radius 26'' the total brightness of Echeclus plus its coma was determined to be  $r'_T = 15.98 \pm 0.05$  mag. Using the method described above, the flux of the nucleus and coma were disentangled and their brightnesses were respectively calculated to be  $r'_N = 16.89 \pm 0.05$  mag and  $r'_C = 16.62 \pm 0.05$  mag.

Here we recognise that the coma's contribution to the flux is likely underestimated, and consequently the nucleus flux is overestimated. This is largely because our stellar SBP is broader than that of Echeclus at small values of  $\rho$ , and that flux from the near-nucleus coma is undersampled. Additionally, with only a single stellar source from which to measure the stellar PSF and the poor flat-fielding of the image, our estimated coma flux values and magnitudes very likely have larger uncertainties than those quoted here. As a result the subsequent estimates for  $Af\rho$  and the mass of the dust ejected by the outburst are quoted merely at order-of-magnitude precision.

The parameter  $Af\rho$  is designed to be a measure of the quantity of solar radiation reflected by cometary dust

grains that is independent of observing geometry and the width of the field of view (A'Hearn et al. 1984).  $Af\rho$  has significant limitations, as explained in detail by Fink & Rubin (2012). Echeclus' asymmetric coma and lack of ongoing activity puts our observations beyond the limitations within which  $Af\rho$  should reasonably be applied. Nevertheless,  $Af\rho$  can still serve as a useful proxy for the size of an outburst, and in the interest of comparability between this and previous works (Bauer et al. 2008; Rousset 2008; Rousset et al. 2016) we have calculated  $Af\rho$  using the standard equation (e.g. see Mazzotta Epifani et al. 2007),

$$Af\rho = \frac{(2r_H\Delta)^2}{\rho} 10^{-0.4(r'_C - r'_{\odot})}. \quad (1)$$

We calculated  $Af\rho$  for an aperture with radius of 26'' (equivalent to  $\sim 10^{10}$  cm at Echeclus) and obtained a value for  $r'_{\odot}$  from Willmer (2018). We also applied the phase angle correction of Schleicher et al. (1998), although Echeclus was observed at a small phase angle of 0.9454° and this correction is negligible within our large uncertainty margin. At order-of-magnitude precision we found  $Af\rho \sim 10^2$  cm, a value much smaller than

the  $Af\rho \sim 10^4$  cm estimate made by Bauer et al. (2008) and Rousselot (2008) for Echeclus' large 2005–2006 outburst, but comparable to the values of  $Af\rho$  estimated for the outburst of 2011 (Rousselot et al. 2016).

We estimated the solar flux reflected by a single dust grain in Echeclus' coma by rearranging the following equation (Russell 1916) to solve for  $F_D$ ,

$$p = \frac{2.25 \times 10^{22} \Delta^2 r_H^2}{r_D^2} \frac{F_D}{F_\odot}, \quad (2)$$

where  $\Delta = 5.35$  au,  $r_H = 6.35$  au, and  $r'_\odot = -26.93$  (Willmer 2018), which corresponds to a flux,  $F_\odot = 1.7 \times 10^5$  erg s<sup>-1</sup> cm<sup>-2</sup>. We assumed the grain's albedo,  $p$ , to be the same as that of Echeclus (0.052; Duffard et al. 2014), and that the grains observed in the image were in the Mie resonant scattering regime (see Hapke 2012) with radius,  $r_D = 0.5$   $\mu$ m. From this we estimated the reflected flux from a single grain to be  $F_D = 8.5 \times 10^{-35}$  erg s<sup>-1</sup> cm<sup>-2</sup>. The measured coma magnitude of  $r'_C = 16.62$  corresponds to a flux,  $F_C = 6.6 \times 10^{-13}$  erg s<sup>-1</sup> cm<sup>-2</sup>. A lower limit to the number of dust grains in Echeclus' coma was calculated to be  $N = F_C/F_D \sim 8 \times 10^{21}$ . Assuming spherical dust grains with a density of  $\sim 1 \times 10^3$  kg m<sup>-3</sup> as measured by the GIADA instrument onboard Rosetta (Rotundi et al. 2015), we estimate a lower limit on the total mass of Echeclus' dust coma to be of order  $\sim 10^6$  kg.

## 5. DISCUSSION

### 5.1. *Echeclus*

Despite evidence that cometary outbursts should change the reflectance properties of a centaur, including that gathered in-situ at comet 67P (Filacchione et al. 2016a) and from laboratory experiments (Poch et al. 2016a,b), we have not observed any change in the reflectance spectrum of Echeclus as a result of its 2016 outburst. We have not found any direct evidence to suggest the removal of an irradiated surface crust or the uncovering of fresh subsurface ices and silicates as predicted by Delsanti et al. (2004) and Doressoundiram et al. (2005); this process should have manifested in the spectrum as the appearance of NIR absorption bands and the likely shallowing of the visual and NIR spectral gradients. Due to Echeclus' unchanging visual and NIR spectral gradients we also report no evidence for the blanketing of redder surface material by more neutral material falling back from the coma as predicted by Jewitt (2002, 2009, 2015).

A simple explanation for the lack of change in Echeclus' spectrum may be that the outburst was not large enough to expose much of Echeclus's subsurface. Even on the much more active JFC 67P, it was found

that the largest changes were localised to the most active regions of the nucleus surface (Filacchione et al. 2016a). If changes were localised to a small area they may not have been observable in our spatially unresolved measurements. In a similar vein, even though some of the blue material from Echeclus' coma likely fell back to the nucleus, it has clearly not been enough to significantly alter the visual properties of Echeclus' surface as observed from Earth.

It is unlikely that any large regions of exposed subsurface material could have been transformed by heat and irradiation from the Sun to be indistinguishable from the rest of Echeclus in only six weeks. Crystalline water ice is thermodynamically stable at  $>5$  au and should have been observable if it was present on the Earth-facing side of Echeclus during our observations. Additionally, any irradiation mantle destroyed by activity could not be replaced by the irradiation of simple subsurface organics in the time between outburst and observations. Strazzulla et al. (2003) report that the production of a complex refractory organic crust requires ion irradiation doses of order  $10^2$  eV(16 amu)<sup>-1</sup> based on laboratory experiments. Under the solar wind at heliocentric distances of 5–10 au a surface takes  $\sim 10^2 - 10^3$  years to receive a total ion dose this high (Kaňuchová et al. 2012; Melita et al. 2015). Hence, if a large region of irradiated surface had been destroyed by the outburst to reveal an unirradiated subsurface, we would likely have detected it by changes in Echeclus' spectral slope. While the exposure of volatile ices such as carbon dioxide (CO<sub>2</sub>) to seasonal heating on 67P has been shown to change the local surface composition on a timescale of weeks (Filacchione et al. 2016b), our observations would imply a rapid disappearance of any potential deposit of volatile ices in any freshly exposed subsurface layers of Echeclus.

### 5.2. *Dust Coma*

The unusually blue reflectance spectrum of Echeclus' dust coma, with a visual slope of  $-7.7 \pm 0.6\%$  per  $0.1 \mu$ m, appears to be unique among active centaurs observed to date. Multiple active centaurs and JFCs, including Echeclus, have been reported to have comae that are more neutrally coloured than the surfaces of their respective nuclei (A'Hearn et al. 1989; Jewitt & Luu 1989; Bauer et al. 2003a, 2008; Rousselot 2008; Jewitt 2009; Fernández et al. 2017); they are, however, typically still redder than solar at visual wavelengths.

In typical cases of activity, Rayleigh scattering is often invoked as a cause for more neutrally coloured comae, especially at larger cometocentric distances where smaller, non-geometrically scattering grains have been thrown off faster and further from the nucleus. Jewitt (2015), how-

ever, argued that while optically small particles are numerically dominant in cometary comae, optically large particles dominate the scattering cross-section, and the neutral/blue colour of coma material is not dominated by small-particle scattering. In the case of Echeclus this interpretation is reinforced by the fact that our observations were performed six weeks post-outburst, after solar radiation pressure has likely dispersed the smallest grains, and those still observable are large enough to remain despite the effects of the solar wind.

If the colour of Echeclus' dust coma is not a scattering effect it may be reflective of the dust's composition, with the best compositional candidate being carbon-rich organic matter. In the lab, amorphous carbon black, carbonaceous chondrites, and Insoluble Organic Matter (IOM) from the Murchison meteorite have been observed to show dark, featureless, blue-sloped reflectance spectra (Cloutis et al. 1994, 2011; Clark et al. 2010). Hydrocarbon and carbon-phase molecular fragments contained in dust particles released by active comets have also been measured or collected in-situ on multiple occasions: at 1P/Halley by the Vega and Giotto missions (Kissel et al. 1986a,b), at 81P/Wild by the Stardust mission (Sandford et al. 2006), and at 67P by multiple instruments on board the Rosetta spacecraft and its lander, Philae (Goesmann et al. 2015; Wright et al. 2015; Fray et al. 2016). Additionally, it was reported by Bardyn et al. (2017) that hydrocarbons are the dominant refractory material in 67P's dust grains, making up 50% of the dust by mass. Hydrocarbons can become dehydrogenated when exposed to photonic and ionic radiation leading to a loss of their red reflectance properties in favour of a more neutral-blue spectrum (Cloutis et al. 1994; Moroz et al. 1998, 2004). This is borne out by studies of amorphous carbon collected at 81P which, if not primordial, was likely created by the breakup of more structured hydrocarbons by ion irradiation (Muñoz Caro et al. 2008; Brunetto et al. 2009). Fomenkova et al. (1994) also found that in the coma of 1P, organic molecules were more abundant near to the nucleus compared to further away, suggesting that they were decomposing in the coma environment. Given that the dust observed and presented in this work had been exposed to direct solar irradiation for around six weeks, it is possible that complex hydrocarbons at the surface of the grains may have been dehydrogenated and broken up, such that the dust grains now have blue featureless reflectance properties dominated by relatively dehydrogenated amorphous carbon.

While composition is a tempting hypothesis to explain the dust's blue colour, there are other ways to produce a blue slope that are worth noting. Laboratory experi-

ments have observed that removal of the smallest particles from samples of CI and CM carbonaceous chondrites produces a bluer reflectance spectrum compared to the original ensemble (Clark et al. 2010; Hiroi et al. 2010; Cloutis et al. 2013). Observations of Murchison IOM have also shown strong bluing effects when observed at low phase angles (Cloutis et al. 2011). Our observations were performed at a low phase angle of  $\sim 0.9^\circ$  and are likely dominated by larger grains; hence, we cannot rule out these effects when considering the colour of Echeclus' dust.

The way in which the dust's reflectance spectrum is blue in the visual, but levels out toward the NIR may have interesting implications for understanding the effects of blanketing that may take place as a result of cometary activity (Jewitt 2002). Mixing enough of this blue dust into the red regolith of an unprocessed centaur would have a much stronger colour neutralising effect at visual wavelengths, while in the NIR the colour may remain largely unchanged. This is something observed in the colours of centaurs, whereby their visual colours are bimodally distributed, but towards the NIR the colour bifurcation is absent (e.g. Peixinho et al. 2015). Also, if the dust's colour is indicative of a low albedo carbon-rich composition, deposition of this dust onto a centaur's surface would likely lower its albedo alongside neutralising its colour. Blanketing by carbon-rich dust of this kind could be a viable way to push a centaur from the higher albedo red colour group into the lower albedo less-red colour group (Lacerda et al. 2014).

## 6. CONCLUSIONS

We have compared VNIR reflectance spectra of 174P/Echeclus covering the 0.4-2.1  $\mu\text{m}$  range from 2014 while Echeclus was inert and six weeks after its 2016 outburst. The high S/N spectra were observed and reduced consistently across both epochs to ensure direct comparability between them. We did not observe any absorption features in Echeclus' spectrum following the outburst, nor have we observed any change in the visual or NIR spectral gradients at a statistically significant level. All our measurements are broadly consistent with those published in previous works. The lack of change in Echeclus' reflectance properties may be attributable to suboptimal observing geometry or possibly that the outburst was not strong enough to cause significant change to the surface such that it would be observable from Earth.

A surprising result of this work is the observation of Echeclus' unusually blue dust coma, which from a reflectance spectrum we measured a visual slope of  $-7.7 \pm 0.6\%$  per 0.1  $\mu\text{m}$  that levels out towards the NIR. From

photometric measurements made post-outburst we also find that the  $g'-r'$  color of the dust is also consistent with being bluer than solar, with  $g'-r' = 0.32 \pm 0.14$ , corroborating our spectroscopic observations. It is unlikely that the blue color of the dust is caused by non-geometric scattering effects, and may in fact be indicative of the carbon-rich composition of the dust, but without discernible absorption features in the dust spectrum this cannot be confirmed. If the colour of the dust is representative of its composition it is possible that deposition of enough of this material on the surface of a centaur may be able to neutralise the centaur's initially red optical colour.

We have also analysed an  $r'$  image obtained during our post-outburst observations. From this we have estimated  $Af\rho \sim 10^2$  cm and a lower limit on the mass of the dust coma of  $\sim 10^6$  kg at this time.

We thank M.G. Hyland for contributing to the data that went into our P97 DDT observing proposal. We also thank the staff at Paranal Observatory for the great effort they put into performing our DDT observations; particular thanks go to G. Beccari, J. Pritchard, and B. Häußler. Spectra used in the P93 observing pro-

posal were reduced using a pipeline written in IDL by G. Becker (described by López et al. 2016). T.S. acknowledges support from the Northern Ireland Department for the Economy, and the Astrophysics Research Centre at Queen's University Belfast. W.C.F. and A.F. acknowledge support from UK Science and Technology Facilities Council grant ST/P0003094/1. T.H.P. acknowledges support through FONDECYT Regular Grant No. 1161817 and CONICYT project Basal AFB-170002. This work is based on observations collected at the European Organisation for Astronomical Research in the Southern Hemisphere under ESO programs 093.C-0259(A) and 297.C-5064(A). This research made use of NASA's Astrophysics Data System Bibliographic Services, the JPL HORIZONS web interface (<https://ssd.jpl.nasa.gov/horizons.cgi>), and data and services provided by the IAU Minor Planet Center.

*Facilities:* ESO VLT(X-Shooter)

*Software:* astropy (Astropy Collaboration et al. 2013), ESO Reflex (Freudling et al. 2013), matplotlib (Hunter 2007), numpy (van der Walt et al. 2011), scipy (Jones et al. 2001), SExtractor (Bertin & Arnouts 1996) TRIPPy (Fraser et al. 2016), The X-Shooter Pipeline (Modigliani et al. 2010)

## REFERENCES

A'Hearn, M. F., Campins, H., Schleicher, D. G. & Millis, R. L. 1989, *ApJ*, 347, 1155

A'Hearn, M. F., Schleicher, D. G., Millis, R. L., Feldman, P. D. & Thompson, D. T. 1984, *AJ*, 89, 579

Abolfathi, B., Aguado, D. S., Aguilar, G., et al. 2018, *ApJS*, 235, 42

Alvarez-Candal, A., Fornasier, S., Barucci, M. A., de Bergh, C. & Merlin, F. 2008, *A&A*, 487, 741

Astropy Collaboration, Robitaille, T. P., Tollerud, E. J., et al. 2013, *A&A*, 558, A33

Bardyn, A., Baklouti, D., Cottin, H., et al. 2017, *MNRAS*, 469, S712

Barucci, M. A., Belskaya, I. N., Fulchignoni, M. & Birlan, M. 2005, *AJ*, 130, 1291

Bauer, J. M., Choi, Y. J., Weissman, P. R., et al. 2008, *PASP*, 120, 393

Bauer, J. M., Fernández, Y. R. & Meech, K. J. 2003a, *PASP*, 115, 981

Bauer, J. M., Meech, K. M., Fernández, Y. R., et al. 2003b, *Icarus*, 166, 195

Bertin, E., & Arnouts, S. 1996, *A&AS*, 117, 393

Boehnhardt, H., Delsanti, A., Barucci, A., et al. 2002, *A&A*, 395, 297

Brunetto, R., Pino, T., Dartois, E., et al. 2009, *Icarus*, 200, 323

Choi, Y. J., Weissman, P. R. & Polishook, D. 2006, *IAUC*, 8656

Choi, Y. J., Weissman, P. R., Chesley, S., et al. 2006, *CBET*, 563

Clark, B. E., Ziffer, J., Nesvorný, D., et al. 2010, *JGR*, 115, E06005

Cloutis, E. A., Gaffey, M. J. & Moslow, T. F. 1994, *Icarus*, 107, 276

Cloutis, E. A., Hiroi, T., Gaffey, M. J., Alexander, C. M. O'D. & Mann, P. 2011, *Icarus*, 212, 180

Cloutis, E. A., Hudon, P., Hiroi, T., et al. 2013, in *Lunar and Planetary Science XLIV*, Abstract #1550

Delsanti, A., Hainaut, O., Jourdeuil, E., et al. 2004, *A&A*, 417, 1145

Di Sisto, R. P. & Brunini, A. 2007, *Icarus*, 190, 224

Dones, L., Gladman, B., Melosh, H. J. et al. 1999, *Icarus*, 142, 509

Doressoundiram, A., Peixinho, N., Doucet, C., et al. 2005, *Icarus*, 174, 90

Duffard, R., Pinilla-Alonso, N., Ortiz, J. L., et al. 2014, *A&A*, 568, A79

Duncan, M., Levison, H. F., & Dones, L. 2004 in Comets II ed. Festou, M. C. et al. (Tucson, AZ; Arizona University Press), 193

Fernández, J. A., Licandro, J., Moreno, F., et al. 2017, *Icarus*, 295, 34

Fernández, Y. R. 2009, *Planet. Space Sci.*, 57, 1218

Filacchione, G., Capaccioni, F., Ciarniello, M., et al. 2016, *Icarus*, 274, 334

Filacchione, G., Raponi, A., Capaccioni, F., et al. 2016, *Sci*, 354, 1563

Fink, U. & Rubin, M. 2012, *Icarus*, 221, 721

Fitzsimmons, A., Snodgrass, C., Rozitis, B., et al. 2018, *NatAs*, 2, 133

Flewelling, H. A., Magnier, E. A., Chambers, K. C., et al. 2016, arXiv, 1612.05243, in preparation

Fomenkova, M. N., Chang, S. & Mukhin, L. M. 1994, *GeCoA*, 58, 4503

Fraser, W. C., Alexandersen, M., Schwamb, M. E., et al. 2016, *AJ*, 151, 158

Fray, N., Bardyn, A., Cottin, H., et al. 2016, *Nature*, 538, 72

Freudling, W., Romaniello, M., Bramich, D. M. et al. 2013, *A&A*, 559, A96

Gladman, B., Marsden, B. G. & VanLaerhoven, C. 2008, in The Solar System Beyond Neptune, ed. Barucci, M. A. et al. (Tucson, AZ; Arizona University Press), 43

Goesmann, F., Rosenbauer, H., Bredehöft, J. H., et al. 2015, *Sci*, 349, aab0689

Gomes, R. S., Fernández, J. A., Gallardo, T. & Brunini, A. 2008 in The Solar System Beyond Neptune, ed. Barucci, M. A. et al. (Tucson, AZ; Arizona University Press), 259

Guilbert, A., Alvarez-Candal, A., Merlin, F., et al. 2009, *Icarus*, 201, 272

Hapke, B. 2012, Theory of Reflectance and Emittance Spectroscopy (2nd ed; New York, NY: Cambridge University Press)

Hardorp, J. 1980, *A&A*, 91, 221

Hiroi, T., Jenniskens, P. M., Bishop, J. L. & Shatir, T. 2010, in Lunar and Planetary Science XLI, Abstract #1148

Horner, J., Evans, N. W. & Bailey, M. E. 2004, *MNRAS*, 354, 798

Hunter, J. D. 2007, *CSE*, 9, 3

Jaeger, M., Prosperi, E., Vollmann, W., et al. 2011, *IAUC*, 9213

Jewitt, D. 2009 *AJ*, 137, 4296

Jewitt, D. 2015 *AJ*, 150, 201

Jewitt, D. C. 2002 *AJ*, 123, 1039

Jewitt, D. & Luu, J. 1989, *AJ*, 97, 1766

Jones, E., Oliphant, T., Peterson, P. et al. 2001, SciPy: Open source scientific tools for Python, <http://www.scipy.org/>

Kaňuchová, Z., Brunetto, R., Melita, M. & Strazzulla, G. 2012, *Icarus*, 221, 12

Kissel, J., Sagdeev, R. Z., Bertaux, J. L., et al. 1986, *Nature*, 321, 280

Kissel, J., Brownlee, D. E., Buchler, K., et al. 1986, *Nature*, 321, 336

Kulyk, I., Korsun, P., Rousselot, P., Afanasiev, V. & Ivanova, O. 2016, *Icarus*, 271, 314

Lacerda, P., Fornasier, S., Lellouch, E., et al. 2014, *ApJL*, 793, L2

Lamy, P. & Toth, I. 2009, *Icarus*, 201, 674

Levison, H. F. & Duncan, M. J. 1997, *Icarus*, 127, 13

López, S., D'Odorico, V., Ellison, S. L., et al. 2016, *A&A*, 594, A91

Luu, J. X. & Jewitt D. 1996, *AJ*, 122, 2310

Martayan, C., Mehner, A., Beccari, G., et al. 2014, *Msngr*, 156, 21

Mazzotta Epifani, E., Palumbo, P., Capria, M. T., et al. 2007, *MNRAS*, 381, 713

Melita, M., Kaňuchová, Z., Brunetto, R. & Strazzulla, G. 2015, *Icarus*, 248, 222

Miles, R., Camilleri, P., Birtwhistle, P. & Gonzalez, J. J. 2016, *CBET*, 4313

Modigliani, A., Goldoni, P., Royer, F., et al. 2010, *Proc. SPIE*, 7737, 28

Moffat, A. F. J. 1969, *A&A*, 3, 455

Moroz, L., Baratta, G., Strazzulla, G., et al. (2004), *Icarus*, 170, 214

Moroz, L. V., Korochantsev, A. V. & Wäsch, R. 1998, *Icarus*, 134, 253

Muñoz Caro, G. M., Dartois, E. & Nakamura-Messenger, K. 2008, *A&A*, 485, 743

Peixinho, N., Delsanti, A. & Doressoundiram, A. 2015, *A&A*, 577, 35

Peixinho, N., Doressoundiram, A., Delsanti, A., et al. 2003, *A&A*, 410, L29

Perna, D., Barucci, M. A., Fornasier, S., et al. 2010, *A&A*, 510, 53

Poch, O., Pommierol, A., Jost, B., et al. 2016, *Icarus*, 266, 288

Poch, O., Pommierol, A., Jost, B., et al. 2016, *Icarus*, 267, 154

Rotundi, A., Sierks, H., Della Corte, V., et al. 2015, *Sci*, aaa3905

Rousselot, P. 2008, *A&A*, 480, 543

Rousselot, P., Korsun, P. P., Kulyk, I., Guilbert-Lepoutre, A. & Petit, J.-M. 2016, MNRAS, 462, S432

Rousselot, P., Petit, J.-M., Poulet, F. & Sergeev, A. 2005, Icarus, 176, 478

Russell, H. N. 1916, ApJ, 43, 173

Sandford, S. A., Aléon, J., Alexander, C. M. O'D., et al. 2006, Sci, 314, 1720

Schleicher, D. G., Millis, R. L. & Birch, P. V. 1998, Icarus, 132, 397

Scotti, J. V., Gleason, A. E., Montani, J. L. & Read, M. T. 2000, MPEC 2000-E64

Seccull, T., Fraser, W. C., Puzia, T. H., Brown, M. E. & Schönebeck, F. 2018, ApJL, 855, L26

Smette, A., Sana, H., Noll, S., et al. 2015, A&A, 576, A77

Stansberry, J., Grundy, W., Brown, M., et al. 2008, in The Solar System Beyond Neptune, ed. Barucci, M. A. et al. (Tucson, AZ; Arizona University Press), 161

Strazzulla, G., Cooper, J. F., Christian, E. R. & Johnson, R. E. 2003, CRPhy, 4, 791

Tegler, S. C., Bauer, J. M., Romanishin, W. & Peixinho, N. 2008, in The Solar System Beyond Neptune, ed. Barucci, M. A. et al. (Tucson, AZ; Arizona University Press), 105

Tiscareno, M. S. & Malhotra, R. 2003, AJ, 126, 3122

van der Walt, S., Colbert, S. C. & Varoquaux, G. 2011, CSE, 13, 22

Vernet, J., Dekker, H., D'Orico, S. et al. 2011, A&A, 536, A105

Vernet, J., Kerber, F., Mainieri, V., et al. 2010, HiA, 15, 535

Weissman, P. R., Chesley, S. R., Choi, Y. J. et al. 2006, BAAS, 38, 551

Wierzchos, K., Womack, M. & Sarid, G. 2017, AJ, 153, 230

Willmer, C. N. A. 2018, ApJS, 236, 47

Wright, I. P., Sheridan, S., Barber, S. J., et al. 2015, Sci, 349, aab0673